Coupled Pattern Analysis of Sea Surface Temperature and TOPEX/Poseidon Sea Surface Height

ERIC W. LEULIETTE* AND JOHN M. WAHR

Department of Physics and CIRES, University of Colorado, Boulder, Colorado

(Manuscript received 10 April 1997, in final form 14 May 1998)

ABSTRACT

Though thermal effects dominate steric changes in sea level, the long-period contribution of thermal expansion to sea level is uncertain. Nerem et al. found that a global map of sea surface temperature (SST) trends and a corresponding map of TOPEX/Poseidon-derived sea surface height (SSH) trends were strongly correlated. This result is explored with a coupled pattern analysis (CPA) between five years of global SST and SSH, which allows for matching of modes of common temporal variability.

The dominant mode found is an annual cycle that accounts for nearly all (95.3%) of the covariance between the fields and has a strong SST/SSH spatial correlation (0.68). The spatial correlation is strong in both the Atlantic (0.80) and the Pacific (0.70). Good temporal and spatial agreement between the SSH and SST fields for the primary seasonal mode suggests that a robust regression between fields may have some physical significance with respect to thermal expansion and that the regression coefficient might be a proxy for the mixing depth of the mode. The value of the regression coefficient, H, scaled by a thermal expansion coefficient of 2×10^{-4} °C^{-1} is 40 m for this mode, and ranges from 33 to 47 m among the basins.

The primary mode of a nonseasonal CPA is an interannual mode that captures 38.0% of the covariance and has significant spatial correlations (0.54) between SSH and SST spatial patterns. The spatial pattern and temporal coefficients of this mode are correlated with ENSO events. A robust regression between fields finds that the nonseasonal modes have a regression coefficient 2–4 times that of the seasonal modes, indicative of deeper thermal mixing. The secondary nonseasonal mode captures most of the secular trend in both fields during the period examined. The temporal coefficients of this mode lag those of primary mode. Evidence is presented that this mode is consistent with the behavior expected from secular trends that are dominantly forced by thermal expansion.

1. Introduction

Steric changes in sea level at global scales are dominated by thermal effects. Freshwater and salinity fluxes are less important, though they can be significant locally (Pattullo et al. 1955). At long wavelengths sea surface temperature is a reasonable proxy for the thermal content of the mixed layer, with regions of notable exceptions such as the Southern Ocean and the intertropical convergence zone. A secular increase in sea surface temperature should be accompanied by a rise in global steric height. For example, Wigley and Raper (1987) estimated that while the global mean temperature increased by ~0.5° from 1880 to 1985, the thermal expansion contribution to sea level rise was 2–5 cm. And by using a model based on the dynamics of subduction and Sverdrup balance, Church et al. (1991) estimated that a global-mean 3.0°C temperature rise by 2050 would produce 20–30 cm of sea level rise.

Operational satellite oceanography now provides global datasets for sea surface height (SSH) and sea surface temperature (SST), which can be used to study thermal effects on sea level at periods of a few years and less. Results from global SST analyses have been available for many years. But continuous and accurate SSH results from satellite altimetry have become available only relatively recently. The TOPEX/Poseidon altimetric satellite, launched in August 1992, has been achieving extraordinary accuracies of better than 5 cm at all spatial scales (Fu et al. 1994; Shum et al. 1995). In particular, the precise determination of the orbit of the TOPEX/Poseidon altimetry mission has allowed for the accurate study of long-wavelength oceanographic features (e.g., Tapley et al. 1994).

Previous studies (Cheney 1982; Khedouri and Szczechowski 1983; Carnes et al. 1990) have found high correlations between altimeter-derived sea surface height and subsurface temperatures. Nerem et al. (1997) report

* Current affiliation: Center for Space Research, Austin, Texas.

Corresponding author address: Dr. E. W. Leuliette, Center for Space Research, 3925 W. Braker Lane, Suite 200, Austin, TX 78759-5321.
E-mail: leuliette@csr.utexas.edu

that the correlation between a global map of SST trends and a corresponding map of TOPEX/Poseidon-derived SSH trends during 1993–96 is 0.6. They suggest that this correlation may be evidence of sea level rise due to heat storage near the surface of the ocean. However, they note that some of the correlation may be attributable to indirect causes, primarily water displacements due to wind stress, presumably from ENSO-related variability.

Here, we extend this type of comparison by considering the spatial structure of the SSH/SST relationship at seasonal and interannual periods. We use a global coupled pattern analysis to compare five years of TOPEX/Poseidon-derived SSH and optimally interpolated SST. For intercomparison, the global analysis was sampled for each of the three ocean basins (Pacific, Atlantic, and Indian) to calculate key parameters.

2. Coupled pattern analysis

The enormous complexity of global meteorological and oceanographic datasets has lead to the increasing use of objective analysis methods to help in their interpretation. Probably the most familiar methods used for analyzing a single field involve empirical orthogonal functions (EOFs).

In an EOF analysis, a temporally and spatially varying field, $\mathbf{s}(x, t)$ (such as either SSH or SST), is expanded as a sum of orthogonal, spatially dependent functions, $\mathcal{L}_k(x)$:

$$\mathbf{s}(x, t) = \sum_{k=1}^{N} a_k(t)\mathcal{L}_k(x), \tag{1}$$

where the coefficients $a_k(t)$ are time-varying functions and N is the number of spatial points x. If $\mathbf{s}(x, t)$ is SSH, for example, then (1) is analogous to a standing wave expansion of the ocean's surface. The shape of a ''wave'' is described by $\mathcal{L}_k(x)$, and the ''wave's'' time dependence is $a_k(t)$. There are many possible ways of constructing an orthogonal set of $\mathcal{L}_k$. In EOF analyses, the $\mathcal{L}_k$ are chosen to be eigenfunctions of the $N \times N$ temporal covariance matrix:

$$S(x, x') = \sum_{t} \mathbf{s}(x, t)\mathbf{s}(x', t). \tag{2}$$

The eigenvalue associated with $\mathcal{L}_k$ turns out to be equal to the fraction of the total variance of $\mathbf{s}(x, t)$ [the sum over space and time of $\mathbf{s}(x, t)^2$] contributed by the term $a_k(t)\mathcal{L}_k(x)$ in the expansion (1).

For real data, most of the terms $a_k(t)\mathcal{L}_k(x)$ in (1) are usually mathematical artifacts with little, if any, physical significance. But there are usually a few terms where $\mathcal{L}_k$ has a particularly large eigenvalue, indicating that an unusually large fraction of the field is organized coherently into that spatial pattern. Those terms are then extracted for further analysis and interpretation.

EOF and related analyses of SST at regional and global scales have been described in numerous studies (e.g., see Weare et al. 1976; Weare 1977, 1979; Hsiung and Newell 1983; Hu et al. 1994; Kawamura 1994). Similar analyses have been applied to altimetry data from both the Geosat Exact Repeat Mission and the TOPEX/Poseidon satellite (White and Tai 1992; Zou and Latif 1994; Hendricks et al. 1996). All of these analysis methods have drawbacks, which can be mostly traced to the lack of a physical basis for the decomposition (Mitchum 1993). On the other hand, the total independence of any a priori prejudice of what to expect is perhaps their greatest strength.

One approach that has been used to investigate thermal effects on sea level is to compare EOFs for SSH and SST. However, when multiple fields are analyzed separately, it can be difficult to identify related modes. This problem can be reduced by using singular value decomposition of the covariance of two geophysical fields. This technique provides an objective method of isolating coupled modes of variability between the fields, and has been in use in meteorology for two decades (Prohaska 1976; Lanzante 1984). Here we adopt the coupled pattern analysis method and notation of Bretherton et al. (1992).

Coupled pattern analysis is similar in spirit to EOF analysis. Two fields, $\mathbf{s}(x, t)$ and $\mathbf{z}(x, t)$, are expanded into sums of orthonormal modes as in (1):

$$\mathbf{s}(x, t) = \sum_{k=1}^{N} a_k(t)\mathcal{L}_k(x) \tag{3a}$$

$$\mathbf{z}(x, t) = \sum_{k=1}^{N} b_k(t)\mathcal{R}_k(x), \tag{3b}$$

where we will assume here that both fields are defined on the same spatial grid of N points (this assumption is not necessary). In our applications, $\mathbf{s}(x, t)$ will represent SSH and $\mathbf{z}(x, t)$ will represent SST. In coupled pattern analysis, the orthonormal, spatially dependent functions $\mathcal{L}_k(x)$ and $\mathcal{R}_k(x)$ are chosen to be the right and left singular vectors of the cross-covariance matrix:

$$C(x, x') = \sum_{t} w(x)w(x')\mathbf{s}(x, t)\mathbf{z}(x', t)/\tau, \tag{4}$$

where τ is the number of observations and $w(x)$ is a latitude-dependent weighting suggested by North et al. (1982) to produce an equal-area weighting. Then $C(x, x')$ can be expanded in terms of these singular vectors as

$$C(x, x') = \sum_{k=1}^{N} \sigma_k \mathcal{L}_k(x)\mathcal{R}_k^{\mathrm{T}}(x'), \tag{5}$$

where σ_k is the singular value associated with $\mathcal{L}_k$, $\mathcal{R}_k$ and is nonnegative. Note from (5) that, since both $\mathcal{L}_k$ and $\mathcal{R}_k$ are orthonormal sets, then

$$C\mathcal{R}_k = \sigma_k \mathcal{L}_k \tag{6a}$$

$$C^{\mathrm{T}}\mathcal{L}_k = \sigma_k \mathcal{R}_k. \tag{6b}$$

Equations (6) imply that $\mathcal{L}_k$ and $\mathcal{R}_k$ are eigenvectors of

CC^{T} and $C^{\mathrm{T}}C$, respectively, and that σ_k^2 is the eigenvalue for both these eigenvectors. It can be shown that there are at most $\tau - 1$ values of σ_k^2 that are nonzero.

The intent of coupled pattern analysis is to find pairs of "standing wave" patterns, one for $\mathbf{s}(x, t)$ and one for $\mathbf{z}(x, t)$, that have similar temporal dependence and that contribute significantly to the data. When the method described above is used to find these pairs of patterns, $\mathcal{L}_k$ and $\mathcal{R}_k$, the covariance between their temporal coefficients is $\Sigma_t\, a_k(t)b_k(t)$, which reduces to σ_k. Thus if a pair of patterns corresponds to a large singular value, the covariance between their temporal coefficients is large. There is no enforced criterion, however, that the two spatial patterns must look alike. If a mode with a large singular value has patterns for $\mathbf{s}(x, t)$ and $\mathbf{z}(x, t)$ that are similar, it tends to reinforce the suggestion that the mode truly does reflect some sort of linear physical connection between the two fields. The spatial correlation between the two patterns,

$$r_{\text{space}} \equiv \frac{\sum_x \mathcal{L}_k(x)\mathcal{R}_k(x)}{\sqrt{\sum \mathcal{L}_k^2(x) \sum \mathcal{R}_k^2(x)}}, \tag{7}$$

is a measure of their similarity. However, there could also be a physical connection, even if the two patterns are different since cause and effect need not be local.

The statistical significance of the individual modes has proven difficult to quantify (Wallace 1992). We have adopted an ad hoc method to provide a rough estimate of the significance of the spatial correlations r_{space}. The confidence levels for r_{space} depend on the number of degrees of freedom ν. Because the fields of SSH and SST tend to be coherent over long periods and long wavelengths, using the standard assumption that ν is related to the number of data points N, as $\nu = N - 2$, would greatly overstate the case. To ameliorate this deficiency, we sought to reduce the degrees of freedom to account for the spatial coherence of the fields. We assumed that the first modes of maximum covariance found by the coupled pattern analysis (CPA) include most of the spatially coherent signal. The fields were reconstructed using (3), successively eliminating the first few modes. To be conservative, the more coherent field, SST, was used to calculate the average spatial correlations versus distance in both longitude and latitude.

For each reconstruction, the average e-folding distance, the distance required for the amplitude to decrease by $1/e$, was calculated along lines of longitude and latitude. As expected, the average e-folding distance dropped as the dominant modes were eliminated from the reconstructions. Eliminating the first six modes (91%–95% of the covariance) excluded the significant coherent modes. Using this reconstruction, we estimated the degrees of freedom, $\tilde{\nu}$, to be the number of data points divided by the e-folding distances in number of grid points in longitude and latitude. To estimate the 99% confidence levels for r_{space} of the first five modes, the reconstructed $\tilde{\nu}$ values were used in a Student's t-distribution with the following results: global $\tilde{\nu} = 209$, $r_{\text{space}}(99\%) = 0.16$; Pacific $\tilde{\nu} = 128$, $r_{\text{space}}(99\%) = 0.20$; Atlantic $\tilde{\nu} = 85.7$, $r_{\text{space}}(99\%) = 0.25$; and Indian $\tilde{\nu} = 80.1$, $r_{\text{space}}(99\%) = 0.26$. For the results with the seasonal terms removed from both datasets (section 3a), the confidence levels were estimated to be global $\tilde{\nu} = 234$, $r_{\text{space}}(99\%) = 0.15$; Pacific $\tilde{\nu} = 141$, $r_{\text{space}}(99\%) = 0.19$; Atlantic $\tilde{\nu} = 87.4$, $r_{\text{space}}(99\%) = 0.25$; and Indian $\tilde{\nu} = 90.9$, $r_{\text{space}}(99\%) = 0.24$.

A number of other functions have been defined to characterize the significance of each mode. For example, the total squared covariance is $\Sigma_{x,x'} C(x, x')C(x, x')$, which can be shown to equal $\Sigma_{k=1}^{\tau} \sigma_k^2$. Thus, the squared covariance fraction,

$$\text{SCF}_k \equiv \frac{\sigma_k^2}{\sum_{l=1}^{\tau-1} \sigma_l^2}, \tag{8}$$

is a measure of the fraction of the total squared covariance explained by the kth pair of patterns, and will be our primary means of identifying significant modes.

However, there can be some ambiguity in the interpretation of SCF values. A mode described by $\mathcal{L}_k(x)$ and $\mathcal{R}_k(x)$ can make a large contribution to the total squared covariance if the temporal coefficients $a_k(t)$ and $b_k(t)$ are well correlated, but also if either $a_k(t)$ or $b_k(t)$ is especially large. For example, suppose we are comparing SST and TOPEX/Poseidon SSH data. And suppose we do not remove an adequate tide model from the SSH results so that the SSH residual field, $\mathbf{s}(x, t)$, has a large remaining tidal signal. In such cases we have found that the coupled pattern analysis can produce modes that are dominated by the tidal signal and have large SCF values. Clearly these modes do not describe any causal physical relationship because the SST data do not contain any obvious tidal signals. In this case the analysis will construct a mode by extracting a spurious time dependence from the SST data that has a small amplitude but happens to look reasonably similar to the tidal SSH time dependence. Because the tidal variance in the SSH signal is large, the mode provides a substantial contribution to the total squared covariance even though the corresponding SST signal is small.

One way of helping to identify problems of this sort is to consider the temporal correlation coefficient

$$r_{\text{time}} \equiv \frac{\sum_t a_k(t),\, b_k(t)}{\sqrt{\sum a_k^2(t) \sum b_k^2(t)}}. \tag{9}$$

Because of its denominator $\sqrt{\Sigma\, a_k^2(t)\, \Sigma\, b_k^2(t)}$, r_{time} is not inflated as much by large, spurious modes as is the SCF. The tidal modes described above are still apt to give seemingly large values of r_{time} since the analysis technique does extract a tidelike time dependence from the

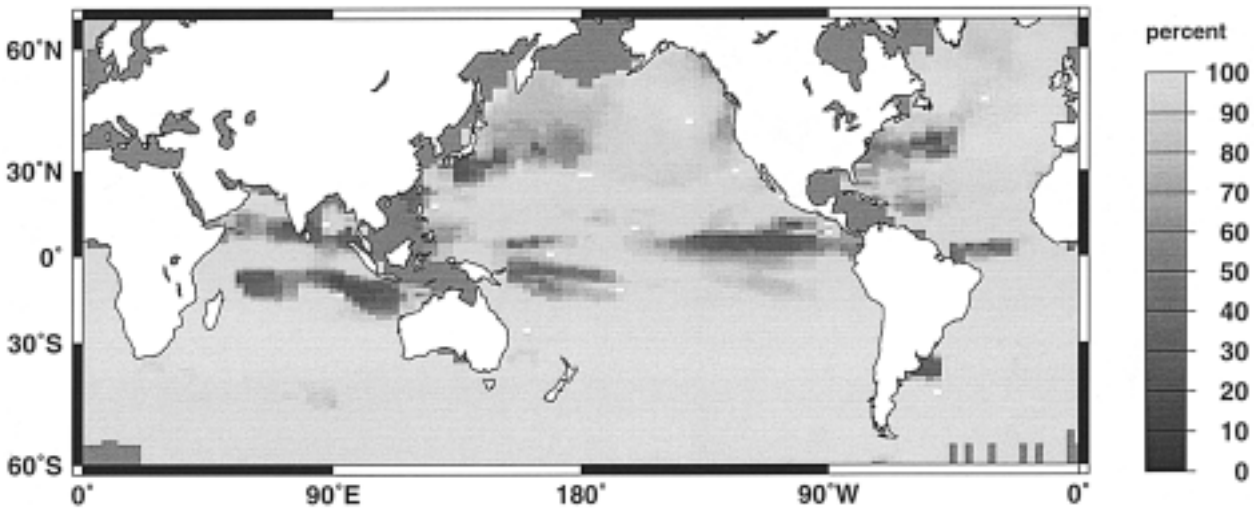

FIG. 1. The relative spatial contributions of the weights used in a robust regression between the primary seasonal mode.

SST data. But these r_{time} values are not as large relative to those of other modes, as ranked by the SCF. Thus, it is often possible to identify a spurious mode by looking to see if there is a dip in its value of r_{time} relative to those of other modes that have comparable values of SCF.

Because strong spatial correlations between the mode patterns $\mathcal{L}_k(x)$ and $\mathcal{R}_k(x)$ tend to suggest a causal relationship, we compute r_{space} (7) for each mode. For modes with large values of SCF and with strong temporal and spatial correlations, the regression coefficient between the modes provides a measure of coupling between the fields. These regression coefficents are indicative of the depths of top-layer mixing required to produce the thermal expansion seen the modes. To determine this coefficient we have used the method of weighted least squares analysis, a ''robust'' regression, because there are regions in each basin where thermal expansion is clearly not the dominant process and they should be treated as outliers in the regression.

The method of the least median of squares deviation (LMS) was used to determine the weightings for a least squares fit (Rousseeuw 1984; Rousseeuw and Leroy 1987). The least median of squares deviation determines the coefficient $\tilde{A}_k$ that minimizes the median of $r_{x,t}^2$ over x, t, where

$$r_{x,t} = a_k(t)\mathcal{L}_k(x) - \tilde{A}_k[b_k(t)\mathcal{R}_k(x)]. \tag{10}$$

To scale A to a depth, we define

$$H = A/\alpha, \tag{11}$$

where α is a thermal expansion coefficient, 2×10^{-4} °C^{-1}.

To determine the outliers of this regression, the residuals are compared to an empirically determined robust scale estimate of the data,

$$\hat{\sigma} = C\sqrt{\underset{x,t}{\text{median}}\, r_{x,t}^2}, \tag{12}$$

where $C = 1.4826$ is an asymptotic correction factor for the case of normally distributed residuals, which scales $\hat{\sigma}$ to be equivalent to the rms of residuals. Data with residuals exceeding a strict cutoff are weighted with zero:

$$w_{x,t} = \begin{cases} 1, & \text{if } |r_{x,t}/\hat{\sigma}| \le 2.5 \\ 0, & \text{if } |r_{x,t}/\hat{\sigma}| > 2.5. \end{cases} \tag{13}$$

The weightings produced from the LMS were applied to (10) for a standard least squares fit that minimizes $(w_{x,t}r_{x,t})^2$ over x, t to produce A_k, which have units of mm/°C.

The distribution of the weightings used in determining the regression coefficient averaged over all cycles for the primary seasonal mode is illustrated in Fig. 1. Areas with the least weighting are mainly the western boundary currents and some equatorial regions. These weightings exclude most regions where Stammer (1997) found large residual differences between annually varying T/P SSH anomalies and a steric estimate.

3. Data preparation

Sea surface height values were derived from cycles 10 through 195 of the TOPEX/Poseidon mission. Altimeter data from cycles 10–183 were provided by Generation B Merged Geophysical Data Records. The data from TOPEX cycles 184–195 were calculated from Geophysical Data Records, processed to be equivalent to the MGDR-Bs. The initial cycles of the mission were discarded due to pointing errors (Fu et al. 1994). Standard corrections were applied including the wet and dry troposphere, ionosphere, and inverted barometer. The

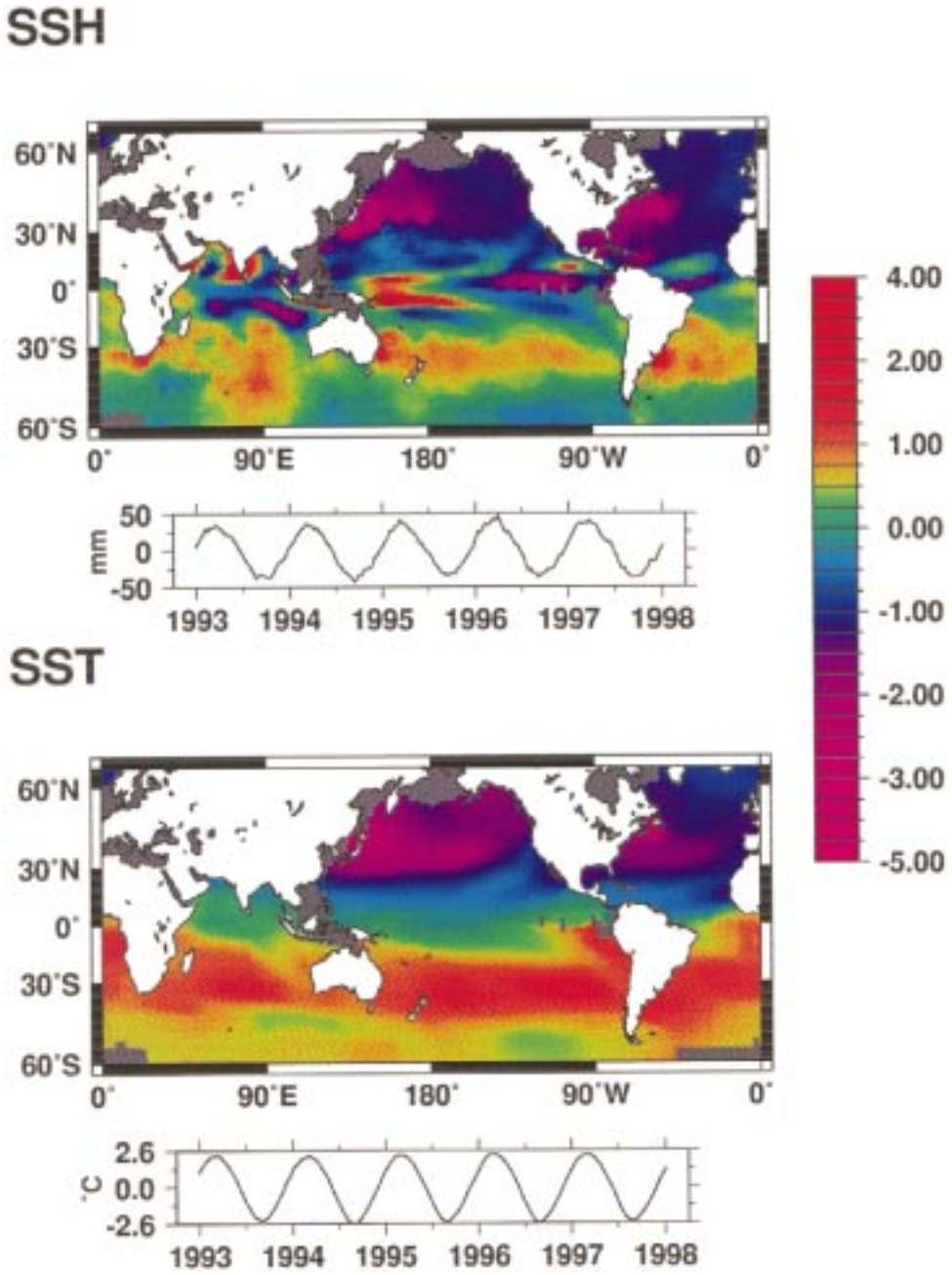

FIG. 2. The principal coupled seasonal mode of SST and SSH. SST patterns, $\mathcal{L}_k(t)$, and SSH patterns, $\mathcal{R}_k(t)$, are depicted as color maps. The associated expansion coefficients $a_k(t)$ and $b_k(t)$ are shown as line plots.

TABLE 1. The principal seasonal modes. The estimated 99% significance level of r_{space} is 0.16.

Mode	SCF (%)	σ^2_{SSH} (mm^2)	σ^2_{SST} (°C^2)	r_{space}	r_{time}	A (mm °C^{-1}, m)
S1	95.3	703 (12.9%)	2.86 (85.2%)	0.68	0.95	7.9
S2	1.8	384 (7.0%)	0.10 (3.1%)	0.28	0.94	6.6

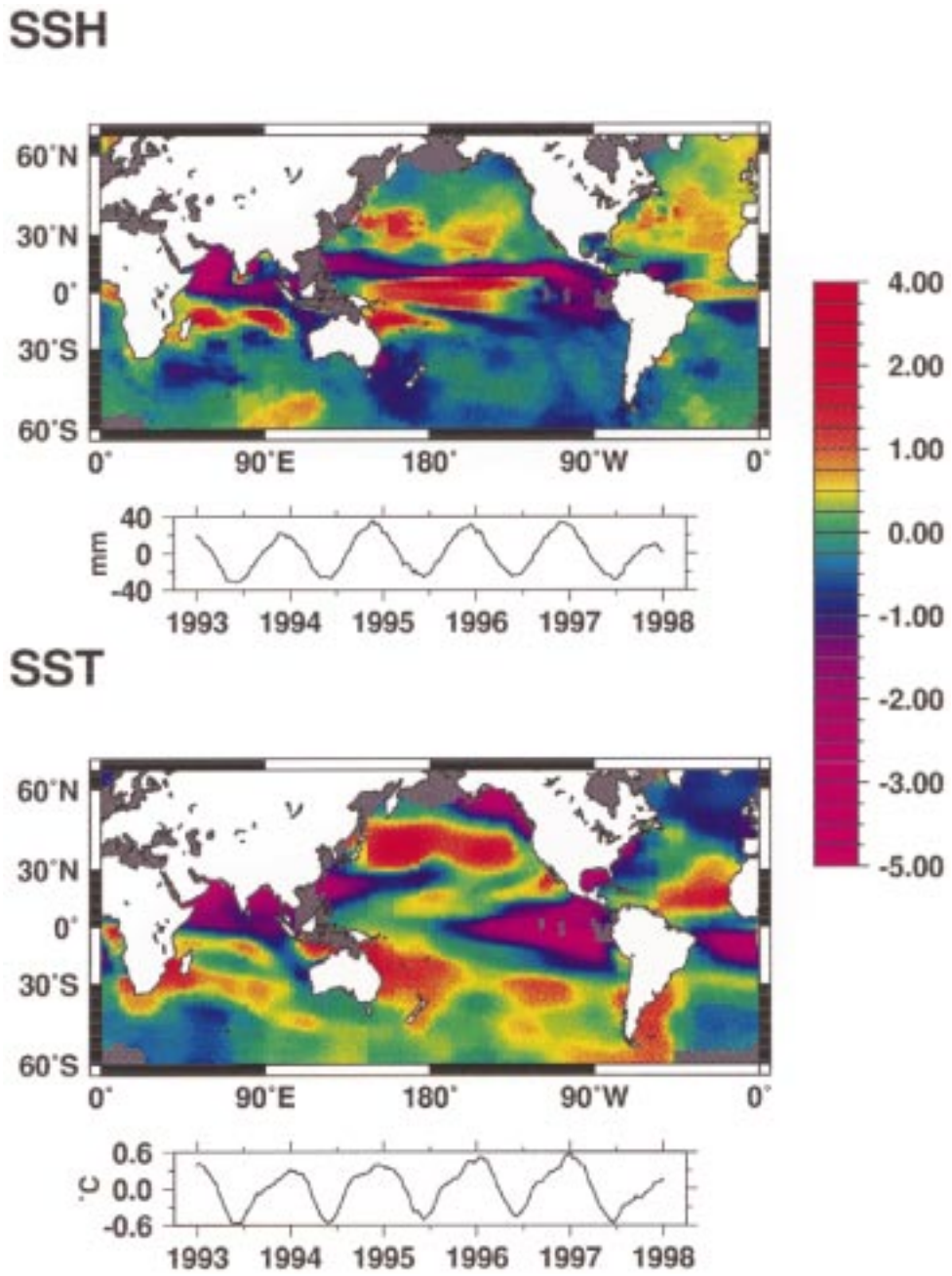

FIG. 3. Same as Fig. 2 except depicting the second seasonal coupled mode.

latest available Desai and Wahr (1995) empirical tide model was removed. In addition, an altimeter range stability estimate (Hayne et al. 1994) was removed from each cycle. No orbit-error correction was attempted. A mean sea level, constructed by averaging these cycles together, was removed from the data to produce the anomalous values used to construct the covariance matrix defined in (4).

The SST field used was the National Centers for Environmental Prediction (NCEP) global analysis. This field is a blend of data from surface marine observations and from the Advanced Very High Resolution Radiometers on the U.S. National Oceanic and Atmospheric Administration's polar-orbiting satellites (Reynolds and Smith 1994). These optimum interpolated datasets are provided as weekly maps on a 1° lat × 1° long spatial grid.

Calculation of a covariance matrix for coupled pattern analysis requires that two fields be sampled simultaneously. To create datasets of SSH and SST evenly sam-

TABLE 2. The principal seasonal coupled modes sampled for each basin. The estimated 99% significance levels of r_{space} for the Pacific, Atlantic, and Indian basins are 0.20, 0.25, and 0.26, respectively.

Mode	r_{space}	A (mm °C^{-1})
Pacific S1	0.70	7.9
Pacific S2	0.27	6.6
Atlantic S1	0.80	9.4
Atlantic S2	0.17	8.6
Indian S1	0.58	6.7
Indian S2	0.32	20.9

pled in time and space we adopted a gridding scheme based on characteristics of the TOPEX/Poseidon orbit. The time sampling used for both fields was the 9.9156-day exact repeat period of the orbit. The choice of spatial grid for both fields was determined by the uneven sampling of the TOPEX/Poseidon ground track. The spatial extent of the grid was limited in two ways. First, to eliminate seasonal aliasing, only regions continuously free of ice were included. Second, since the best available empirical tide models suitable for correcting the altimeter data were less accurate near the coasts, only regions with bathymetry greater than 200 m were included. The data were further restricted to the central basins by eliminating all adjacent seas except for the Bay of Bengal and the Arabian Sea.

Our computing capacity limited the size of the covariance matrices that we can decompose. This in turn limited the size of the boxes used to constuct the spatial maps. Using the 127 orbits in each repeat cycle to determine the longitudinal size of each box, $360°/127 \approx 2.835°$, allowed ascending and descending tracks to be averaged, smoothing some high-frequency variability. The latitudinal resolution of the boxes was 1.25° (≈150 km) and ranged to latitudes of 66.25°, near the maximum latitude of the TOPEX/Posedion ground track.

A box was included in the altimetry gridding only if it included at least 10 samples per cycle. To approximate even temporal sampling, height values were weighted by the fraction of a repeat cycle between the sample and the cycle midpoint. The final grid included only those boxes containing values in 90% of the cycles. A linear interpolation filled in the remaining missing cycles.

Weekly SST analyses were gridded with a bilinear interpolation to produce maps with the same spatial grid as the altimetry data. These maps were linearly interpolated to the sampling rate of the TOPEX/Poseidon exact repeat cycles.

In this study, we have compared SSH and SST data both before and after least squares fitting annual and semiannual terms and removing them from each grid point in both datasets.

4. Results

a. Results prior to removing seasonal terms

The principal coupled mode (Fig. 2 and the S1 mode in Table 1) has seasonal variability that lags the solar heating cycle by about three months, similar to the results of Levitus (1984). This mode explains nearly all (95.3%) of the temporal covariance between the SSH and SST fields. The Pacific and Atlantic exhibit strong SSH/SST spatial correlations (0.70, 0.80; see Table 2) as compared to the 99% confidence levels discussed in section 2 (0.20, 0.25). Visible inspection of the spatial maps of this mode indicates that the major exceptions to these correlations are along the equatorial regions. The Indian Ocean has a lower spatial correlation (0.58), probably due in part to anticorrelations from the freshwater fluxes associated with monsoons.

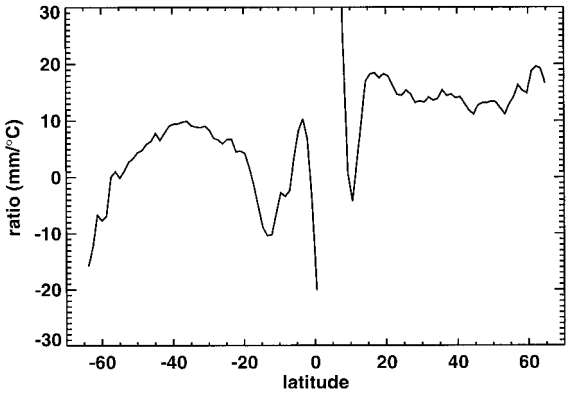

FIG. 4. The regression coefficient A least squares fit at each latitude in mode S1.

The second mode, which captures seasonal variability that is out-of-phase with mode S1, is found in Fig. 3 and summarized as the S2 mode in Table 1. The SSH and SST maps are clearly different in character from each other for mode S2. The SSH mode shows zones of convergence and divergence in the equatorial and Northern Hemisphere. The SST mode is dominated by wind-driven effects: the Kuroshio Extension, symmetrical equatorial-trapped waves near the eastern boundaries, and upwellings along Baja California and the South American coast are coherent large-scale features. The only notable common features in the Atlantic mode are corresponding regions on the eastern boundary near equatorial and southern Africa, including areas of known upwelling.

When a CPA was made using a shorter time series, the S2 mode included semiannual variability. Five years of data appears to be sufficient to separate the seasonal signal completely into separate modes. The seasonal variability in SSH captured in modes S1 and S2 is very similar to the topography found by Nerem and Schrama (1994) and Hendricks et al. (1996).

Our general conclusions are that the in-phase seasonal mode, S1, probably represents the direct effects of surface warming and cooling, but that the physical significance of the out-of-phase seasonal mode is not clear. The good temporal and spatial agreement between the SSH and SST fields in the Atlantic and Pacific for the primary S1 mode suggests that the regression coefficient A, scaled

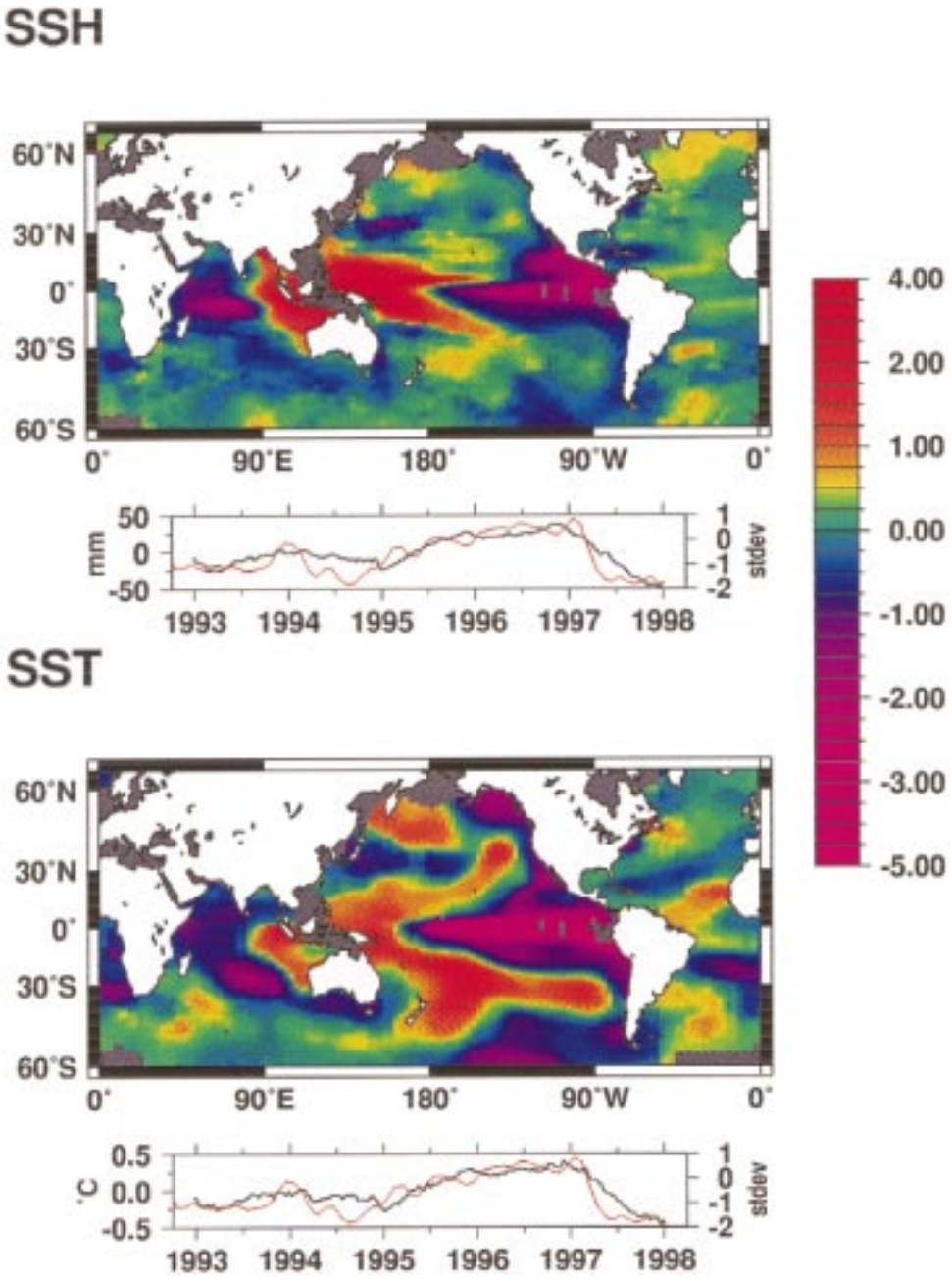

FIG. 5. The primary coupled nonseasonal mode with expansion coefficients $a_k(t)$ and $b_k(t)$ (right column black line plots) that are highly correlated with the Southern Oscillation index (red line overplotted).

TABLE 3. The principal nonseasonal coupled modes of SSH and SST. The estimated 99% significance level of r_{space} is 0.15.

							Trend (yr^{-1})	
Mode	SCF (%)	σ^2_{SSH} (mm^2)	σ^2_{SST} ($°C^2$)	r_{space}	r_{time}	A (mm $°C^{-1}$)	SSH (mm)	SST (°C)
NS1	38.0	359 (8.6%)	0.04 (12.8%)	0.54	0.98	31.9	0.12	−0.0065
NS2	22.2	253 (6.1%)	0.04 (6.1%)	0.39	0.97	27.3	1.13	0.0483
NS3	9.0	179 (4.3%)	0.02 (4.3%)	0.30	0.96	15.2	0.00	0.0058
NS4	6.7	167 (4.0%)	0.02 (4.0%)	0.32	0.96	17.3	−0.12	0.0022
NS5	3.9	143 (3.4%)	0.01 (3.4%)	0.32	0.93	19.0	0.04	0.0006

as a depth H [using (11)], may have some physical significance. The global value of H for this mode is 40 m and ranges from 33 to 47 m among the basins.

Similar to the results noted by Hendricks et al. (1996) and Stammer (1997), we find that SSH variability is stronger in the Northern Hemisphere. SST variability is more evenly partitioned between the hemispheres, and therefore the values of A are higher at northern latitudes, indicating that the seasonal heat uptake is larger than corresponding latitudes south of the equator. Further, the values are more consistent in the Northern Hemisphere north of 15°N, which can be seen in unweighted least squares fits of A at each latitude (Fig. 4), where the values range from 12 to 20 mm °C^{-1}. Values of A in Fig. 4 near the equator and south of 50°S are not meaningful since nonsteric effects are important in those locations.

b. Results after removing seasonal terms

Next, seasonal terms were fit and removed from both datasets, and the coupled pattern analysis was repeated. The primary nonseasonal coupled mode is shown in Fig. 5. The spatial correlations of the primary (NS1) and secondary (NS2) modes are significant under the criteria discussed in section 2 (see Tables 3–4) with large fractions of SCF and significant values of r_{space}. The regression coefficients, A, for leading modes with significant spatial correlations are typically 2–4 times larger than for the principal seasonal modes.

The primary and secondary modes isolate large-scale spatial features with interannual periods. Rossby waves appear to dominate the Pacific (Chelton and Schlax 1996) in the primary mode. The Gulf Stream recirculation gyre is prominent in the secondary mode.

In the primary mode, NS1, the temporal coefficients $a_k(t)$ and $b_k(t)$ are significantly correlated with the monthly NOAA Climate Prediction Center Southern Oscillation index (SOI). Sixty months of SOI coincident with the temporal coefficients were smoothed with a 1–2–1 filter to dampen the high-frequency atmospheric signal and then were correlated with each mode. (The SOI is the red line plotted over the SSH temporal coefficient in Fig. 5.) The correlation (0.85) is significant as compared to the Student's t confidence level [$r_{time}(99\%) = 0.31$]. This correlation suggests that this mode is related to the El Niño/Southern Oscillation. The high spatial correlations in these modes are indicative of good correspondence in the extratropics as well as in the equatorial regions.

After obtaining the leading modes, we calculated the secular trend in SSH and SST of each mode with least squares fit of a bias and a trend, and the results are summarized in Table 3. Trends in each of the sampled basins are listed in Table 4. Basin-averaged secular trends were also calculated for the original deseasonalized fields and are listed in Table 5. Comparing the trend of each mode to the basin-averaged trend in the field allowed us to identify the modes that contain the largest contribution to the apparent sea level change during this time period and analyze those modes for contributions of thermal expansion.

TABLE 4. The principal nonseasonal coupled modes sampled for each basin. The estimated 99% significance levels of r_{space} are 0.24, 0.25, and 0.19 for the Indian, Atlantic, and Pacific Oceans, respectively.

Mode	r_{space}	A (mm °C^{-1})	Trend (yr^{-1}) SSH (mm)	SST (°C)
Pacific NS1	0.57	33.3	0.13	−0.0004
Pacific NS2	0.42	30.6	1.02	0.0553
Atlantic NS1	0.33	23.2	0.18	−0.0006
Atlantic NS2	0.46	21.6	1.32	0.0317
Indian NS1	0.56	44.0	−0.17	−0.0073
Indian NS2	0.36	33.3	1.30	0.0606

When a CPA was calculated using four years of data, the primary mode included most of the trend in SSH and SST fields during that period. Adding data from 1997, when an ENSO was strengthening in the Pacific, has eliminated the trend from NS1 and a trend now dominates mode NS2 (Fig. 6 and Table 3). A significant feature in this mode is the variability of North Atlantic SST, especially in contrast to NS1. Enfield and Mayer (1997) found that 50%–80% of SST variability in the Atlantic between 10°N and 20°N is associated with Pacific ENSO variability, with Atlantic warmings occurring 4–5 months after the mature phases of Pacific warm events. A squared coherency between the temporal coefficients of mode NS1 and mode NS2 shows that these modes are strongly correlated (Fig. 7). A lagged correlation between the temporal coefficients suggests that NS2 lags NS1 by several months (Fig. 8).

Any conclusions that the secondary mode is a delayed response to the primary must be considered preliminary, since the nature of the low-frequency variability in mode NS2 is not clear after only five years of data. Because a coupled pattern analysis empirically isolates modes of covariance in time, it is likely that much of the interannual variability will be isolated into a single mode. Thus, NS2 may represent several phenomena. It is plausible that steric height changes in the Atlantic and long-period thermocline adjustments that lag ENSO could be present simultaneously in this mode.

If all of the variability in a particular nonseasonal mode was caused purely by thermal expansion with a linear response at timescales smaller than the sampling rate of ~10 days, then the ratio of the SSH and SST secular trends in the mode would have the same value as the mode's regression coefficient, A. Thus, comparing these two values in modes that capture significant trends could illuminate the modes in which thermal expansion is the principal dynamic responsible for the secular trend in SSH. We define

$$A_{\text{trend}} = \frac{\text{trend in SSH}}{\text{trend in SST}}. \tag{14}$$

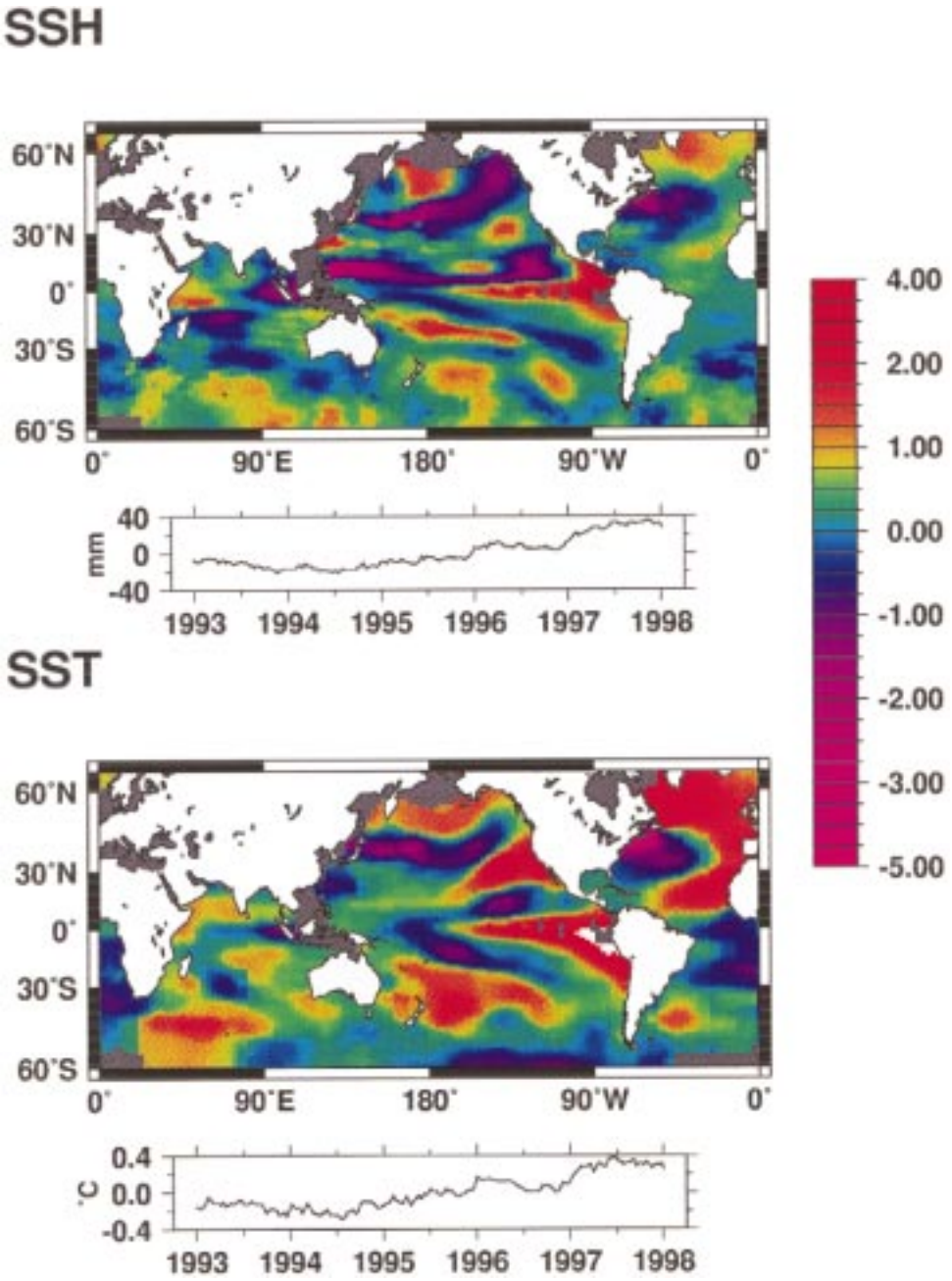

FIG. 6. The secondary coupled nonseasonal mode.

TABLE 5. The secular trends in each basin for the period December 1992–December 1997.

Basin	SSH trend (mm yr^{-1})	SST trend (°C yr^{-1})
Global	1.40	0.057
Pacific	1.50	0.063
Atlantic	1.28	0.043
Indian	1.25	0.066

Indicative of this assumption is the result for the secondary nonseasonal mode, NS2. This mode isolates the bulk of the trends present in the two fields: the mode's secular trend in SSH is 1.13 mm yr^{-1} versus 1.40 mm yr^{-1} of the total field and a secular trend of 0.048 °C yr^{-1} in SST versus 0.57 °C yr^{-1} for the total field. The ratio of the trends in NS2, 23.4 mm °C^{-1}, compares favorably to A value of 27.2 mm °C^{-1}. To test the sensitivity of these two values to the trend in the SSH field, we artificially added 1 mm yr^{-1} of additional trend and recomputed a CPA. In this case the values diverge: the

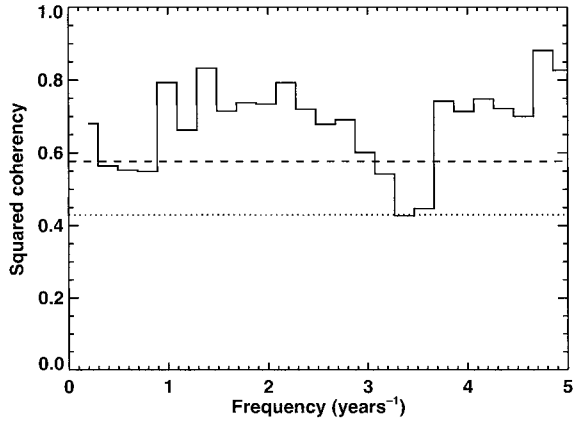

FIG. 7. The squared coherency of the temporal coefficients from modes NS1 and NS2. The dashed line is the 99% confidence level and the dotted line is the 95% level.

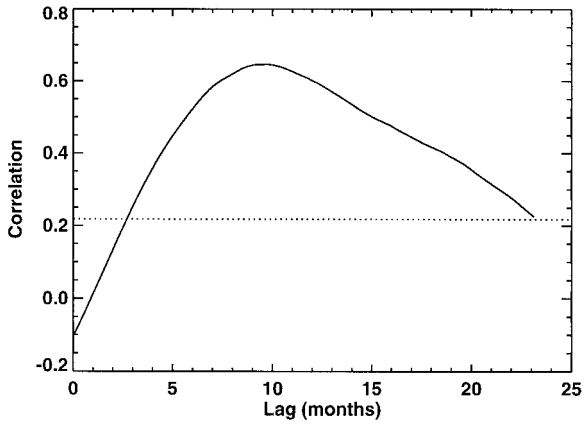

FIG. 8. Lagged correlation of the temporal coefficients of the principal nonseasonal modes, with NS2 lagging NS1. The dotted line is the 99% confidence level.

ratio of secular trends for this mode produce an $A_{\text{trend}} = 39.4$ mm °C^{-1} whereas regression coefficient A rises to only 29.2 mm °C^{-1}. These results are consistent with the behavior that would be expected from secular trends that are predominantly generated by thermal expansion.

5. Conclusions and discussion

The strong temporal and spatial correlations of the primary seasonal mode in the Atlantic and the Pacific provide evidence that these modes capture physically coupled seasonal variability. The major regions of discrepancy are often consistent with known regions of nonthermal density fluxes. Though SST is an imperfect proxy for the thermal content of the mixed layer, the regression estimates of the coupling between the SST and SSH data ($H = 34$–47 m) correspond to plausible mixed-layer thicknesses necessary to produce the observed annually varying steric signal.

In contrast, the out-of-phase mode is not indicative of physical coupling. The relatively poorer spatial correlations indicate that the mode has a large covariance fraction only because of nearly coincident variability. The spatial maps of these modes reflect primarily nonthermal forcing on the oceans.

The regression estimates for the significant nonseasonal modes are generally 2–4 times those of the seasonal modes, indicative of deeper mixing of long-period temperature fluxes. The primary mode exhibits the spatial and temporal characteristics of 1993–97 ENSO variability. Spatial correlations for this mode are stronger in the Pacific and the Indian Oceans.

The secondary nonseasonal mode captures most of the secular trends present in both SST and SSH fields and this mode has a significant SST/SSH spatial correlation, indicating that the source of its variability may be in part a thermal coupling. The ratio of trends in the secondary mode compares favorably to the regression coefficient A, which is consistent with what would be expected from secular trends forced by thermal expansion.

It is somewhat difficult to interpret the coupling coefficients A, especially for the nonseasonal modes. We have attempted to evaluate our results in two ways. First, we calculated the annual amplitude of temperature changes in each layer of the NCEP assimilated model of the Pacific (Behringer et al. 1998). We least squares fit for annual terms in monthly model temperature analyses from 1981 to 1997. Meridional averages of the annual amplitude illustrate that our assumption that annual changes in SSH are largely caused by seasonal warming and cooling of the upper ocean layers is only valid in midlatitudes (Fig. 9). As it happens, when calculating A for the primary mode in the CPA analysis, the equatorial regions were mostly excluded by the robust regression (Fig. 1). Regressions of annual steric height changes from the NCEP model to temperatures at a depth of 5 m yielded values of A ranging from 6 to 14 mm °C^{-1} in the midlatitudes, which is similar to our regression results for the primary seasonal mode (Table 1).

When we look at temperature changes versus depth for the NCEP model results at ENSO periods, we find patterns at most latitudes that more nearly reflect vertical motion of the thermocline (i.e., that resemble the curves for 5° and 10° latitude in Fig. 9), than they do the effects of surface heat flux. Thus, since the NS1 mode appears to be related to the concurrent ENSO, it is probably not appropriate to interpret its regression coefficient in terms of a mixed layer depth.

Second, we compared our results with those of Church et al. (1991). Church et al. separated the ocean into horizontal layers and estimated a thermal sea level rise coefficient for each layer, using an equation of state with data from the Levitus (1982) hydrographic atlas adjusted for the results of climate models. The top layer in their model is a mixed layer with an average depth of 55 m and was estimated to have a coefficient of 11

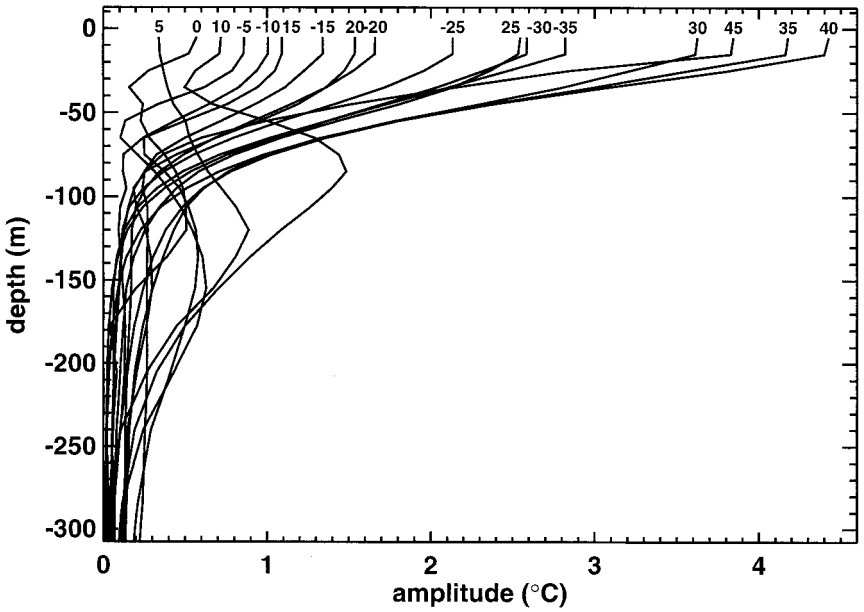

FIG. 9. Zonal averages of annually varying temperature changes in the NCEP model of the Pacific. Numbers at the surface level indicate latitude.

mm $°C^{-1}$. Because this layer has a short residence time, the temperature throughout the layer should closely follow both the seasonal and nonseasonal variations in surface temperature. The mean residence time of the second layer in the Church et al. model was estimated to be 5 yr with an average depth of 141 m and with an expansion coefficient of 19 mm $°C^{-1}$. The longer residence time of this layer means that its temperature and associated thickness are unlikely to vary seasonally, though the layer could conceivably contribute to the longer period SSH variability present in our nonseasonal modes.

Thus, it seems reasonable to compare the 11 mm $°C^{-1}$ sea level rise coefficient for Church et al.'s first layer with our global estimate of 8 mm $°C^{-1}$ for the seasonal S1 mode. These two numbers are comparable. As noted above, our regression results vary with latitude and are larger at latitudes north of 15°N, ranging from 12 to 20 mm $°C^{-1}$.

The regression coefficient for the NS1 mode should probably not be compared with these sea level rise coefficients, for reasons discussed above. But the second mode of our deseasonalized CPA, NS2, may be a combination of ENSO-related variability that has leaked into the solution and thermal expansion of the surface. If we assume the periods of NS2 are long enough that the entire second layer in Church et al.'s model participates in the disturbance, then the NS2 regression coefficient of 27 mm $°C^{-1}$ should be compared with the sum of Church et al.'s sea level rise coefficients for the first two layers: 11 mm $°C^{-1}$ + 19 mm $°C^{-1}$ = 30 mm $°C^{-1}$.

Finally, accuracies of the short, multiyear trends in SSH and SST are active areas of research. For example, differences between sea level averaged over many tide gauges and corresponding TOPEX/Poseidon SSH measurements show a small drift. This drift is believed to originate in the water vapor correction supplied by the TOPEX microwave radiometer (Nerem et al. 1997).

Acknowledgments. We are grateful to S. D. Desai for preparing TOPEX data gridded to a reference track, and to S. Nerem, F. Bryan, T. M. vanDam, and J.-F. Minster for helpful discussion. This work was supported by the TOPEX project at the Jet Propulsion Laboratory under Contract 958126 to the University of Colorado. E.W.L. was partially supported by a 1996 CIRES Graduate Research Fellowship.

REFERENCES

Behringer, D. W., M. Ji, and A. Leetmaa, 1998: An improved coupled model for ENSO prediction and implications for ocean initialization. Part I: The ocean data assimilation system. *Mon. Wea. Rev.,* **126,** 1013–1021.

Bretherton, C. S., C. Smith, and J. M. Wallace, 1992: An intercomparison of methods for finding coupled patterns in climate data. *J. Climate,* **5,** 541–560.

Carnes, M. R., J. L. Mitchell, and P. W. deWitt, 1990: Synthetic temperature profiles derived from Geosat altimetry: Comparison with air-dropped expendable bathythermograph profiles. *J. Geophys. Res.,* **95,** 17 979–17 992.

Chelton, D. B., and M. G. Schlax, 1996: Global observations of oceanic Rossby waves. *Science,* **272,** 234–237.

Cheney, R. E., 1982: Comparison data for Seasat altimetry in the western North Atlantic. *J. Geophys. Res.,* **87,** 3247–3253.

Church, J. A., J. S. Godfrey, D. R. Jackett, and T. R. McDougall, 1991: A model of sea level rise caused by ocean thermal expansion. *J. Climate,* **4,** 438–456.

Desai, S. D., and J. M. Wahr, 1995: Empirical ocean tide models

estimated from TOPEX/Poseidon altimetry. *J. Geophys. Res.*, **100,** 25 205–25 228.

Enfield, B. D., and D. A. Mayer, 1997: Tropical Atlantic sea surface temperature variability and its relation to El Niño–Southern Oscillation. *J. Geophys. Res.*, **102,** 929–945.

Fu, L.-L., E. J. Christensen, C. A. Yamarone Jr., M. Lefebvre, Y. Ménard, M. Dorrer, and P. Escudier, 1994: TOPEX/Poseidon mission overview. *J. Geophys. Res.*, **99,** 24 369–24 381.

Hayne, G. S., D. W. Hancock III, and C. L. Purdy, 1994: TOPEX altimeter range stability estimates from calibration mode data. *TOPEX/Poseidon Research News*, **October,** 18–22. [Available from Jet Propulsion Laboratory, 4800 Oak Grove Drive, Pasadena, CA 91109.]

Hendricks, J. R., R. R. Leben, G. H. Born, and C. J. Koblinsky, 1996: Empirical orthogonal function analysis of global TOPEX/Poseidon altimeter data and implications for detection of global sea level rise. *J. Geophys. Res.*, **101,** 14 131–14 145.

Hsiung, J., and R. E. Newell, 1983: The principal nonseasonal modes of variation of global sea surface temperature. *J. Phys. Oceanogr.*, **13,** 1957–1967.

Hu, W., R. E. Newell, and Z.-X. Wu, 1994: Modes of variability of global sea surface temperature, free atmosphere temperature and oceanic surface energy flux. *Climate Dyn.*, **10,** 377–393.

Kawamura, R., 1994: A rotated EOF analysis of global sea surface temperature variability with interannual and interdecadal series. *J. Phys. Oceanogr.*, **24,** 606–715.

Khedouri, E., and C. Szczechowski, 1983: Potential oceanographic applications of satellite altimetry for inferring subsurface thermal structure. *Oceans 83, Proc. Mar. Technol. Soc.*, 274–280.

Lanzante, J. R., 1984: A rotated eigenanalysis of the correlation between 700 mb heights and sea surface temperatures in the Pacific. *Mon. Wea. Rev.*, **112,** 2270–2280.

Levitus, S., 1982: *Climatological Atlas of the World.* NOAA Prof. Paper No. 13, NOAA, U.S. Department of Commerce, 173 pp.

——, 1984: Annual cycle of temperature and heat storage in the world ocean. *J. Phys. Oceanogr.*, **14,** 727–746.

Mitchum, G. T., 1993: Principal component analysis: Basic methods and extensions. *Statistical Methods in Physical Oceanography*, P. Müller and D. Henderson, Eds., SOEST Special Publication, 185–199.

Nerem, R. S., and E. J. Schrama, 1994: A preliminary evaluation of ocean topography from the TOPEX/Poseidon mission. *J. Geophys. Res.*, **99,** 26 565–26 583.

——, B. J. Haines, J. Hendricks, J. F. Minster, G. T. Mitchum, and W. B. White, 1997: Improved determination of global mean sea level variations from TOPEX/Poseidon altimeter data. *Geophys. Res. Lett.*, **24,** 1331–1334.

North, G. R., F. J. Moeng, T. L. Bell, and R. F. Cahalan, 1982: The latitude dependence of the variance of zonally averaged quantities. *Mon. Wea. Rev.*, **110,** 319–326.

Pattullo, J., W. Munk, R. Revelle, and E. Strong, 1955: The seasonal oscillation in sea level. *J. Mar. Res.*, **14,** 88–155.

Prohaska, J. T., 1976: A technique for analyzing the linear relationships between two meteorological fields. *Mon. Wea. Rev.*, **104,** 1345–1353.

Reynolds, R. W., and T. M. Smith, 1994: Improved global sea surface temperature analyses using optimum interpolation. *J. Climate*, **7,** 929–948.

Rousseeuw, P. J., 1984: Least median of squares regression. *J. Amer. Stat. Assoc.*, **79,** 871–880.

——, and A. M. Leroy, 1987: *Robust Regression and Outlier Detection.* John Wiley & Sons, 329 pp.

Shum, C. K., J. C. Ries, and B. D. Tapley, 1995: The accuracy and applications of satellite altimetry. *Geophys. J. Int.*, **121,** 321–336.

Stammer, D., 1997: Steric and wind-induced changes in TOPEX/Poseidon large-scale sea surface topography observations. *J. Geophys. Res.*, **102,** 20 987–21 009.

Tapley, B. D., and Coauthors, 1994: Precision orbit determination for TOPEX/Poseidon. *J. Geophys. Res.*, **99,** 24 383–24 404.

Wallace, J. M., C. Smith, and C. S. Bretherton, 1992: Singular value decomposition of wintertime sea surface temperature and 500-mb height anomalies. *J. Climate*, **5,** 561–576.

Weare, B. C., 1977: Empirical orthogonal analysis of Atlantic Ocean surface temperatures. *Quart. J. Roy. Meteor. Soc.*, **103,** 467–478.

——, 1979: A statistical study of the relationships between ocean surface temperatures and the Indian monsoon. *J. Atmos. Sci.*, **36,** 2279–2291.

——, A. R. Navato, and R. E. Newell, 1976: Empirical orthogonal analysis of Pacific Ocean sea surface temperatures. *J. Phys. Oceanogr.*, **6,** 671–678.

White, W. B., and C.-K. Tai, 1992: Reflection of interannual Rossby waves at the maritime western boundary of the tropical Pacific. *J. Geophys. Res.*, **97,** 14 305–14 322.

Wigley, T. M. L., and S. C. B. Raper, 1987: Thermal expansion of sea water associated with global warming. *Nature*, **330,** 127–131.

Zou, J., and M. Latif, 1994: Modes of ocean variability in the tropical Pacific as derived from Geosat altimetry. *J. Geophys. Res.*, **99,** 9963–9975.